NJC

ROYAL SOCIETY OF CHEMISTRY

PAPER

View Article Online
View Journal

Cite this: DOI: 10.1039/d5nj02137e

A novel method of SnS_2/Fe_2O_3 composite preparation for use as an asymmetric supercapacitor electrode material

Dost Muhammad,*[a] Syed Hatim Shah,*[b] Amjad A. Almunyif,[c] Sohail Ahmad,[a] Aniqa Jadoon,[a] Nisar Ali,[d] Mohammad M. Al-Hinaai,[d] Rayya Ahmad Al Balushi[d] and Thuraya Al-Harthy[d]

SnS_2 and Fe_2O_3 have attracted a lot of interest because of their superior electrochemical properties as supercapacitor electrode materials. While the low conductivity and poor cycling stability of Fe_2O_3 limit its performance, the strong electrical conductivity and decent theoretical capacity of SnS_2 make it a desirable choice as an additive for composite electrodes. Using a hydrothermal reaction and wet chemical approach, this work successfully fabricates a SnS_2/Fe_2O_3 composite for use as an electrode material in supercapacitors. In contrast to the pure SnS_2 and Fe_2O_3 electrodes, the composite SnS_2/Fe_2O_3 exhibits an expected specific capacitance of 821 F g^{-1} in a three-electrode system. The enhanced specific capacitance of SnS_2/Fe_2O_3 was attributed to its unique surface characteristics and the synergistic interaction between the Sn^{4+} and Fe^{4+} ions. A hybrid supercapacitor was fabricated with SnS_2-based ferric oxide as the cathode and manganese oxide (MnO_2) as the anode. The performance of our fabricated supercapacitor at an elevated voltage of 1.4 V is commendable. Furthermore, a high specific capacitance of 297 F g^{-1} and an energy density of 80.8 W kg^{-1} are attained in a two-electrode ASC using the SnS_2/Fe_2O_3 composite electrode. Furthermore, after 6000 charge/discharge cycles, a suitable capacitive retention of 88% is also reached at 5 A g^{-1}, indicating the high feasibility of the SnS_2/Fe_2O_3 composite in supercapacitors compared to the pristine SnS_2 and Fe_2O_3 samples, which retain 78% and 50%. These findings suggest that the fabricated nanocomposite having a 1 : 1 ratio exhibits remarkable potential for supercapacitor applications.

Received 20th May 2025,
Accepted 26th June 2025

DOI: 10.1039/d5nj02137e

rsc.li/njc

1. Introduction

The rapid pace of technological innovation and societal development has advanced the need for advanced efficiency energy storage devices to support various applications. Consequently, the development of these devices is becoming more urgent and significant. Supercapacitors have garnered significant interest from academia and industry due to their quick charge–discharge rate, admirable rate capability, elevated power density, extended cycle life, and other features. Consequently, supercapacitors are extensively utilised in power tools, hybrid electric vehicles, energy backup systems, and portable electronics.[1–5] Supercapacitors are often classified as electrical double layer capacitors (EDLCs) and pseudocapacitors based on the charge storage process. EDLCs store charge by electrostatically adsorbing electrolyte ions at the electrode–electrolyte interface. Carbon-based materials, including carbon nanotubes (CNTs), activated carbon, and graphene, are frequently utilized as electrode precursors because of their large specific surface area, excellent electrical conductivity, and stable electrochemical processes. However, because of their low energy densities, EDLCs have seen very few practical uses. Quick and reversible pseudocapacitors utilize redox reactions for energy storage inside the electrode. Consequently, because of faradaic redox processes, pseudocapacitors have higher theoretical specific capacities and energy densities than EDLCs.[6,7] The electrode materials play a major role in supercapacitors' ability to function better. Thus, it is imperative to design and synthesize electrode materials with superior electrochemical characteristics. Because of their high theoretical capacity and reversible redox processes, transition metal dichalcogenides (TMDs) and oxides (TMOs) are considered as two significant categories of pseudocapacitance materials. Tin disulfide (SnS_2), one of the several metal oxides,

[a] Faculty of Material Science and Engineering, Kunming University of Science and Technology, Kunming 650093, China. E-mail: dost.muhammad12@gmail.com
[b] Department of Physics, School of Physics and Astronomy, Yunnan University, Kunming, 650504, China
[c] Department of Physics, College of Sciences, Princess Nourah bint Abdulrahman University, P.O.Box 84428, Riyadh 11671, Saudi Arabia
[d] College of Applied Health Sciences, School of Basic and Applied Sciences, A'Sharqiyah University, P.O. Box 42, Ibra P.O. 400, Sultanate of Oman

has drawn a lot of interest as a prospective candidate material because of its many uses.[8] SnS_2 is broadly used for many elevated tech applications, including dye-sensitized solar cells, gas sensors, photocatalysts, lithium-ion batteries, and supercapacitors. These applications are made possible by the exceptional optical and electrical properties, elevated chemical stability, and theoretical capacity of SnS_2.[9–11] TMDs are compounds of scientific interest due to their unique structures, favorable physical characteristics, and natural abundance. Tin disulphide (SnS_2) is the most significant TMD. Additionally, due to its low cost, chemical stability, and environmental friendliness, SnS_2 has shown promise for use in a variety of technologies, including biosensors, dye-sensitized solar cells, Li-ion batteries, and supercapacitors.[12] In the recent past, because of their exceptional qualities, namely their high redox activity and capacity, nanostructured TMOs and TMDs have been considered as most promising electrode materials for supercapacitors.[13] Various SnS_2 nanostructures, including hollow spheres, nanoflakes, nanoflowers and nanosheets, have been created with enhanced electrochemical capabilities.

Consequently, researchers have focused on applying pseudocapacitive materials to carbon electrodes, with the objective of enhancing capacity through pseudocapacitive reactions. Metal sulphides and metal oxides are predominantly utilised as electrochemically active materials in pseudocapacitors. Owing to the significant faradaic redox process, these inorganic materials can provide the desired specific capacitance and further advantages. For instance, Fe_2O_3 is utilised because of its prevalence, affordability, and elevated capacitance, but SnS_2 exhibits superior electrical conductivity and exceptional cycling stability.[14]

Recent studies have indicated that the performance of pseudocapacitors utilizing a singular active component is inadequate. This is due to the fact that a single component fails to provide the requisite features. For instance, Fe_2O_3 exhibits low electronic conductivity, which adversely impacts its electrochemical activity during the reaction process, thereby constraining the performance of the associated pseudocapacitors.[15–17] To address the limitations of the Fe_2O_3 electrode, several nanostructured Fe_2O_3 variants have been suggested to reduce the electrical route over the entire nanostructure. However, this technique is beneficial solely at low operational rates for the Fe_2O_3-based electrode; at high rates, inadequate electronic conductivity remains a significant obstacle that adversely affects the performance of Fe_2O_3. Consequently, certain interests are currently focused on integrating highly conductive compounds with Fe_2O_3. The essential aspect of this design is to identify suitable materials that exhibit high conductivity, capacitance, and effective compatibility with Fe_2O_3 to achieve the optimal performance of the composite.

For both electron transfer and ion diffusion, the nanostructured materials of SnS_2 and Fe_2O_3 offer extended specific surface area, more active sites, and more efficient diffusion paths. Consequently, it is possible to increase the efficiency of active material utilization, leading to an improvement in electrochemical performance, such as cycle life stability and specific capacitance value.[18]

To create SnS_2 and Fe_2O_3 nanostructures, a variety of synthetic techniques could be employed, including chemical bath deposition, microwave-assisted synthesis, the sol–gel method, chemical vapour deposition, and electrodeposition.[19] In comparison to other procedures, the solvothermal method has many advantages because it is easy to use, affordable, and scalable. It is anticipated that the combination of SnS_2 and Fe_2O_3 will endow the electrode material with superior electrochemical performance compared to either of the elements alone.

In this work, flower-like SnS_2 and nanosphere-like Fe_2O_3 outperformed sheet-like SnS_2/Fe_2O_3 (821 F g^{-1}) in terms of specific capacitance, delivered at 1 A g^{-1}. The nanostructured sphere-like Fe_2O_3 was well decorated on the carnation flower-like SnS_2 to create a composite. The morphology of the synthesized nanostructures results in the capacitive characteristics of the produced electrodes. Using electrochemical tests such cyclic voltammetry (CV), galvanostatic charge–discharge, and electrochemical impedance spectroscopy (EIS), the electrochemical performances of the as-synthesized SnS_2 and Fe_2O_3 nanostructures were compared. In this study, the synthesized SnS_2/Fe_2O_3 nano-heterostructures with ratios of 4 : 6 showed improved electrochemical performance. Additionally, after 6000 cycles at a current density of 5 A g^{-1}, the sheet-like SnS_2/Fe_2O_3 demonstrated 88% capacitance retention.

2. Experimental section

2.1 Synthesis of SnS_2, Fe_2O_3 and the SnS_2/Fe_2O_3 composite

The process of generating nano-sized tin sulfide, or SnS_2, entails mixing 40 mL of deionized water with 1.6188 g of $SnCl_4{\cdot}5H_2O$ and 1.6188 g of acetic acid. After that, the mixture is placed on a stirring machine fitted with a magnetic stirrer, 1.14818 g of thioacetamide is added, and the mixture is agitated for 50 min. After that, the resulting clear solution of the combined precursors is heated to 130 °C for 12 h and vacuum-dried at 100 °C for 4 h.

1.8 g of $Fe(NO_3)_3{\cdot}9H_2O$ is dissolved in 30 mL of distilled water to produce Fe_2O_3. After that, $NH_3{\cdot}H_2O$ is added and stirred until the pH reaches 9. After stirring for a further 20 min, the liquid is moved to a 30 mL stainless steel autoclave lined with Teflon. The powder is collected, rinsed multiple times with warm and purified water, and dried for at 70 °C for 12 h to produce the pristine Fe_2O_3 powder and then roasted at 150 °C for 12 h in the oven.

The prepared SnS_2 and Fe_2O_3 are uniformly mixed in a ratio of 4 : 6 in ethanol. The ingredients are ball milled for 8 h at 200 rpm to create SnS_2/Fe_2O_3 composite powders with uniform particle size distribution. The SnS_2/Fe_2O_3 powder is then dried in an oven at 70 °C for 4 h. The preparation methods for the SnS_2, Fe_2O_3, and SnS_2/Fe_2O_3 composite are shown in the accompanying Fig. 1.

3. Characterization of the structure

The structure, morphology, and element composition of each sample were investigated using Tongda TD-3500 X-ray

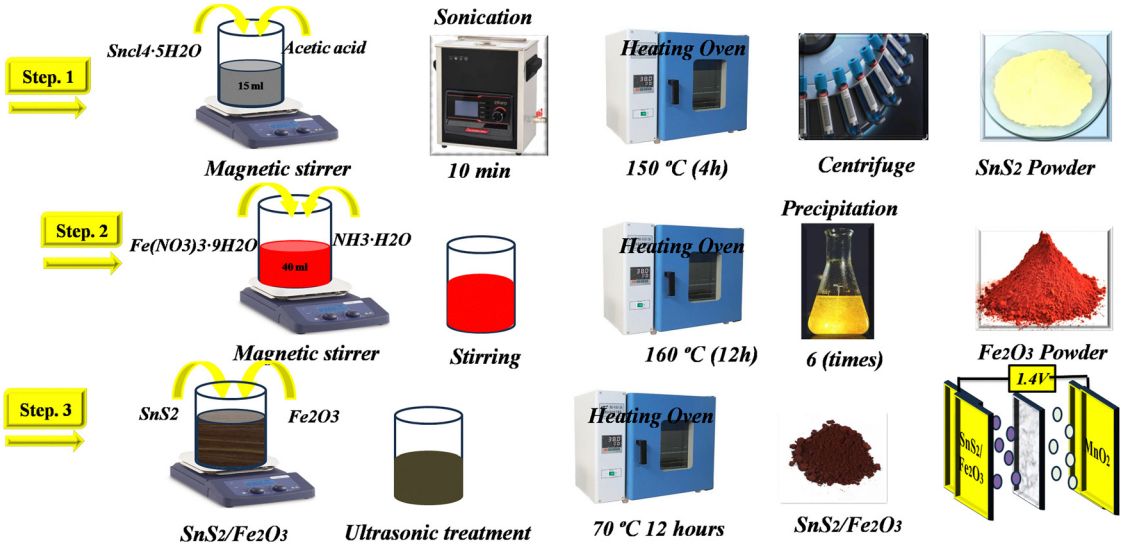

Fig. 1 Synthesis methods used to produce SnS_2, Fe_2O_3, and the SnS_2/Fe_2O_3 composite.

diffraction (XRD), field emission scanning electron microscopy (FESEM), energy-dispersive X-ray (EDX) analysis, and XPS in that order.

3.1. Production and evaluation of the electrode

The relevant mixture of the electrode material, carbon, and polytetrafluoroethylene was pressed into nickel foam at 100 kPa for 2 min to create the SnS_2, Fe_2O_3, and SnS_2/Fe_2O_3-based electrodes. The resulting electrodes were then dried at 60 °C for 4 h (Fig. 2).

Electrochemical impedance spectroscopy (EIS), galvanostatic charge–discharge (GCD), and cyclic voltammetry (CV) measurements were carried out using Princeton Applied Research's PARSTAT 4000 and VersaSTAT 3 (AMETEK) electrochemical workstations to evaluate the electrochemical performance of the SnS_2, Fe_2O_3, and SnS_2/Fe_2O_3 electrodes. In the construction of the three-electrode system, the reference electrode is Hg/HgO, the counter electrode is Pt mesh, and the working electrode is the as-prepared electrode. The following formulas (1)–(3) can be used to calculate the specific capacity (C_s, F g^{-1}), energy density (E, Wh kg^{-1}), and power density (P, W kg^{-1}) of the various materials.[19,20]

$$C_s = \frac{I \times \Delta t}{m \Delta V} \quad (1)$$

$$E = \frac{C_s \times \Delta V^2}{7.2} \quad (2)$$

$$P = \frac{E \times 3600}{\Delta t} \quad (3)$$

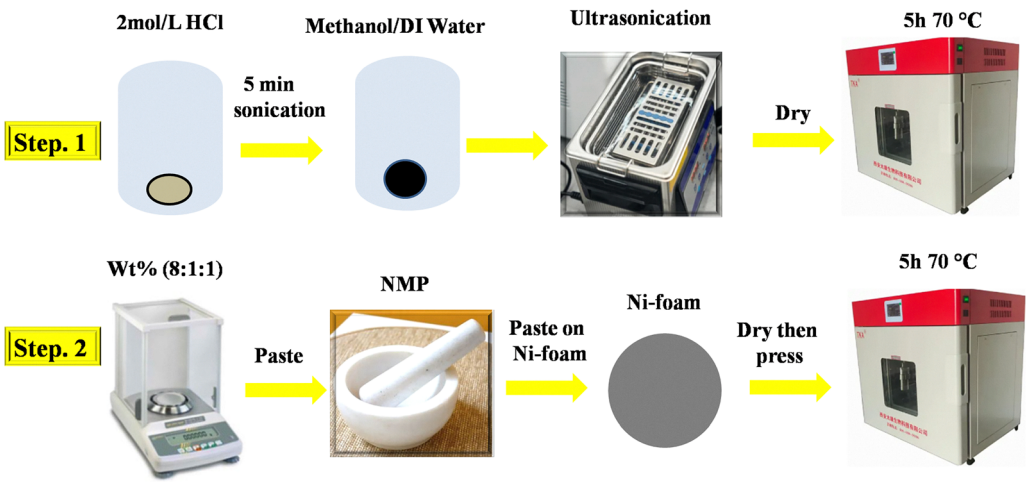

Fig. 2 Schematic diagram showing preparation of the electrodes.

4. Results and discussion

4.1. XRD analysis of the samples

Using a Tongda TD-3500, we performed XRD to analyze the crystal structure of the synthesized materials. The XRD patterns of the SnS_2, Fe_2O_3, and SnS_2-Fe_2O_3 binary composites are displayed in Fig. 3. The fabricated SnS_2 coincides with [JCPDS#83-1705], demonstrating the corresponding peaks at 15.2°, 32.3°, 42.4°, and 50.6°. The results show that the products are highly pure because no impurity diffraction peaks are seen. However, some differences can be seen between the diffraction peaks and the standard data. For example, the intensities of the [001] and [011] peaks are stronger than those in the standard pattern, while the [110] peak intensity is weaker than that of [012]. These differences suggest that all SnS_2 crystals are further restrained in their growth along the "*c*-axis", favoring growth perpendicular to the [001] direction. Additionally, the XRD peaks of the resultant SnS_2 products generally become sharper and stronger as the reaction temperature increases in the same series, suggesting an increase in their crystal sizes. The Fe_2O_3 (Fig. 1(a)) XRD patterns revealed clear peaks at 24.15°, 33.16°, 35.63°, 40.87°, 49.47°, 54.08°, 57.61°, 62.45°, 64.04°, 72.30°, and 75.47°, respectively. The distinctive diffraction peaks found at approximately 24°, 33°, 35°, 49°, and 54° correspond to the (012), (104), (110), (024), and (116) lattice planes of haematite (JCPDS card#79-1741), with negligible impurities detected. The intensity of the (110) plane is plainly greater than that of the other peaks, indicating preferential development of the (110) plane during the crystallization process under hydrothermal treatment. The SnS_2/Fe_2O_3 composite was successfully synthesized, as evidenced by the XRD pattern of the composite, which clearly verifies the coexistence of SnS_2 and Fe_2O_3. Specifically, the crystal and particle sizes were determined using Scherrer's eqn (4).

$$D = \frac{\kappa\lambda}{\beta\sin\theta} \quad (4)$$

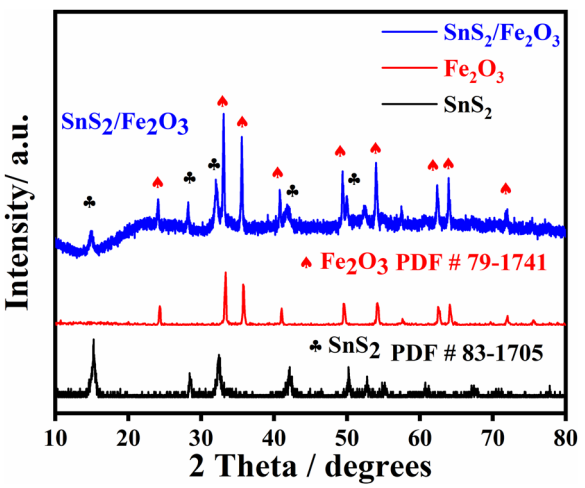

Fig. 3 XRD patterns of FeS, Fe_2O_3 and the FeS/Fe_2O_3 nanocomposite.

Table 1 The crystal parameters of the samples

Sample	Mean crystallite size (nm)	Lattice constant (Å)	Volume (Å)
SnS_2	~55.6	4.7	371.7
Fe_2O_3	~25.7	1.33	311.7
SnS_2/Fe_2O_3	~44.6	3.8	330.6

More specifically, Table 1 lists additional crystal parameters. The average crystal sizes of the SnS_2, Fe_2O_3, and SnS_2/Fe_2O_3 powders were approximately 55.5 nm, 25.7 nm, and 44.6 nm, respectively. As all three particle sizes fall in the same magnitude range, the differences in size are not the primary cause of their differing electrochemical properties.

The nanosphere-like structure of Fe_2O_3 as depicted in Fig. 5(b–b1) and the structural and chemical states of the as-fabricated CF-SnS_2 were investigated using XPS. Fig. 4(a) depicts the entire range of the examined spectra, with binding energies varying from 0 to 1000 eV. The peaks that correspond to the d, p, and s orbitals demonstrate that the as-prepared SnS_2/Fe_2O_3 contains both SnS_2 and Fe_2O_3. For the SnS_2/Fe_2O_3 structure, the Sn 4d states are responsible for the peak at 756.70 eV, the Sn 3d states are responsible for the peaks at 484.74 eV and 493.15 eV, and the S 2p and 2s states are responsible for the peaks at 161.04 eV and 223.87 eV. Fig. 4(b) and (f) show the high-resolution spectra that were utilized to analyze the valence of the Sn 3d and S 2p states. The two strong peaks at around 484.74 and 493.15 eV (Fig. 4(b)) are caused by Sn $3d_{5/2}$ and $3d_{3/2}$, respectively, and are consistent with the presence of Sn^{4+} in SnS_2.[21] Two satellite peaks of the four Fe 2p peaks shown in Fig. 4c are situated at 707.4 eV and 718.6 eV. Fe is divalent, or Fe^{2+}, as shown by the Fe $2p_{1/2}$ and Fe $2p_{3/2}$ peaks at 731.2 eV and 709 eV. Their presence indicates that Fe_2O_3 is present in the composite. The C 1s spectra in Fig. 4e exhibit three peaks at 284.8 eV, 285.8 eV, and 288.7 eV. C–C, C–O, and C═O are responsible for these peaks, respectively. Thus, the SnS_2/Fe_3O_4 combination was effectively synthesized based on the XPS data.

4.2. Component analysis and morphology using EDX and FESEM

FESEM was used to examine the sample morphologies, as seen in Fig. 5a–c. Regarding the FESEM images in Fig. 5, the SnS_2 particles possess an angular appearance with an average size of 110–200 nm, whereas the Fe_2O_3 particles have a sphere-like shape with an average diameter of ~50 nm. With the combination of the two phases, the SnS_2/Fe_2O_3 composite exhibits a morphology that is halfway between spherical and angular bulk, while maintaining a size that is comparable to that of the Fe_2O_3 and SnS_2 nanoparticles. The nanoscale characteristics of the three samples are advantageous for the dynamics of electrochemical reactions and ionic transport in the electrolyte, based on earlier research.[22–24] Furthermore, the composite's somewhat rough surface may increase the electrode's electrochemical active surface area, improving the charging and discharging processes.

Additionally, EDX mapping was performed to make the element distribution in the three samples visible. The composite, as illustrated in Fig. 6(c)–(c4), shows a uniform dispersion of Fe and O due to the larger concentration of Fe_2O_3. The S element in

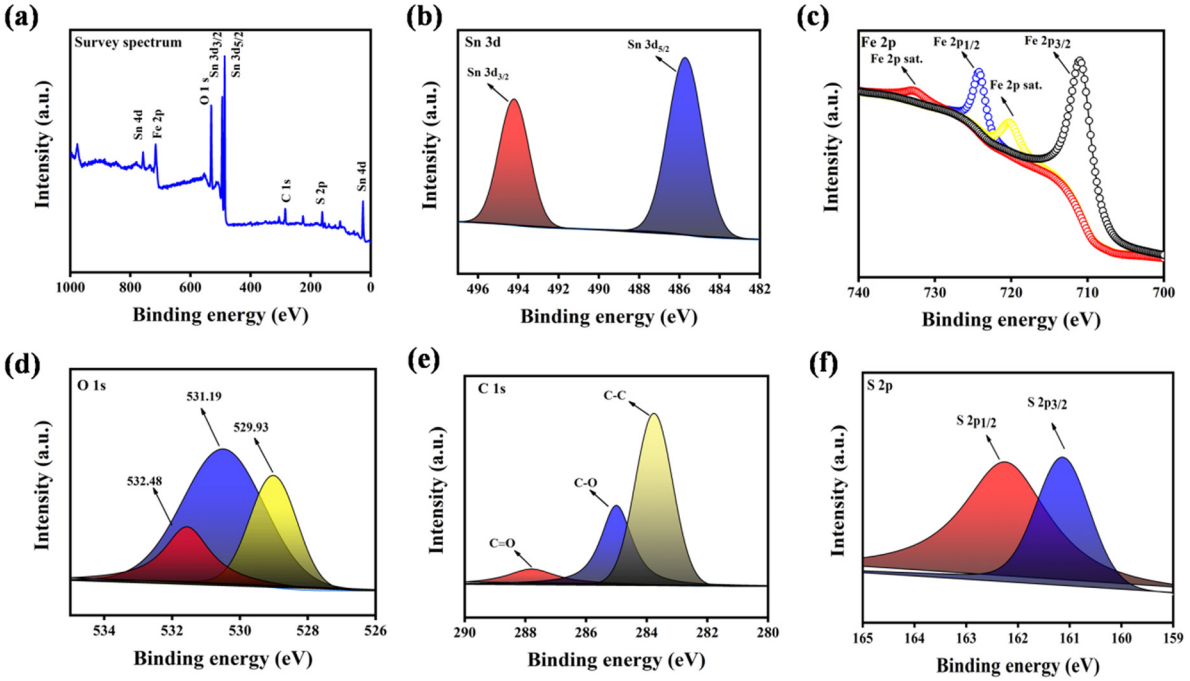

Fig. 4 (a) Wide scan XPS spectra and (b) Fe 2p, (c) O 1s, (d) Sn 3d, (e) C 1s and (f) S 2p spectra of the SnS_2/Fe_2O_3 nanocomposites.

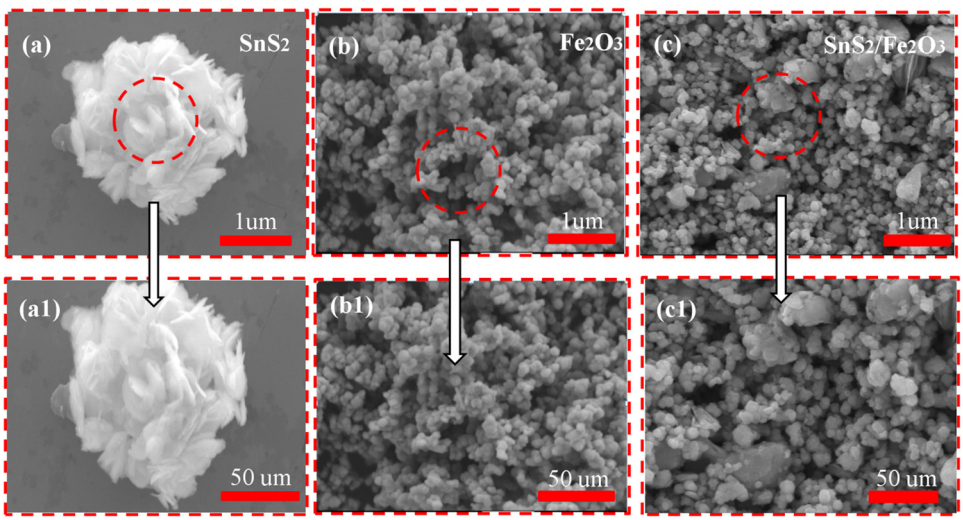

Fig. 5 FESEM images of the (a) SnS_2, (b) Fe_2O_3, and (c) SnS_2/Fe_2O_3 powders.

the composite exhibits a relatively homogenous distribution at the micrometre scale, which is explained by the lower content of SnS_2. The composite appears to be a successful mixture of SnS_2 and Fe_2O_3, when compared to the EDX mappings of pure SnS_2 and pure Fe_2O_3 in Fig. 6(a) and (b).

5. Electrochemical performance tests

First, a three-electrode system was used to compare the electrochemical properties of the SnS_2/Fe_2O_3 composite with those of pure SnS_2 and Fe_2O_3. The related curves and findings are depicted in Fig. 7. Stacked curves of pristine SnS_2 and Fe_2O_3 at various scan rates are generally represented by the SnS_2/Fe_2O_3 graph, indicating that the two phases within the composite have both contributed to the pseudocapacitive process. The CV curve of the SnS_2/Fe_2O_3 composite yields the biggest integrated area among the three samples, suggesting the maximum capacitance, due to the combined contributions of the two components. We specifically selected the curves examined at 90 mV s^{-1} in order to further illustrate the superiority of the SnS_2/Fe_2O_3 composite, as shown in Fig. 7a. The redox reaction between Sn^{4+} and Fe^{3+} is responsible for the single pair of redox peaks that pure SnS_2 and pure Fe_2O_3 exhibit at −0.4 V to −0.3 V, as seen by the curves.

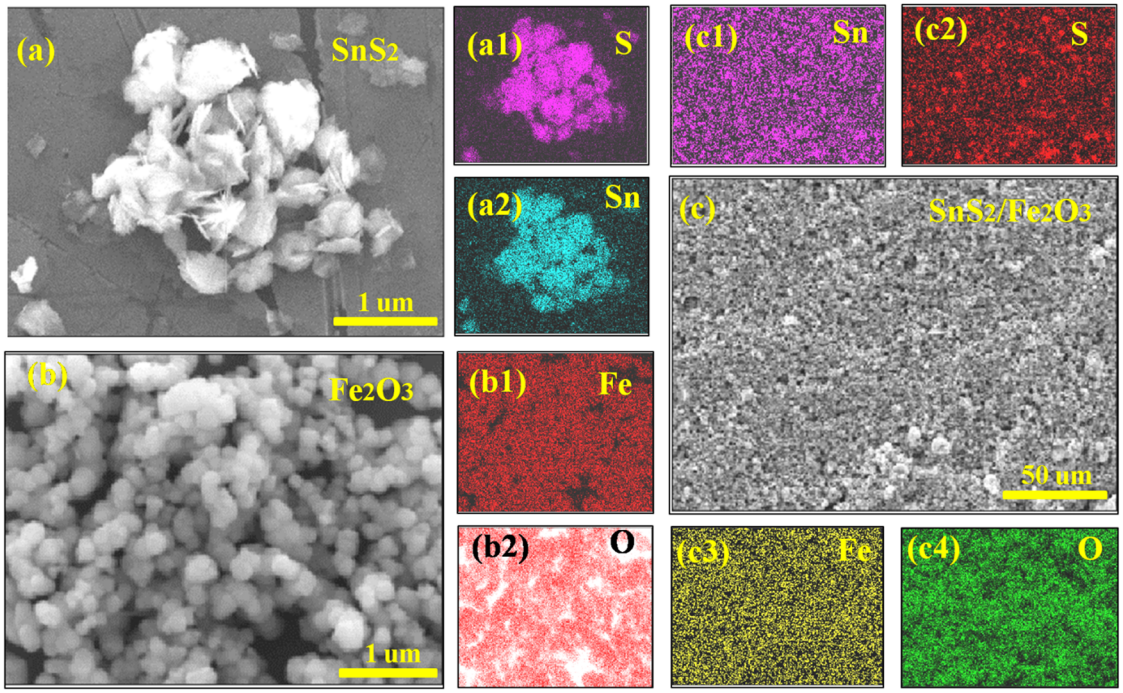

Fig. 6 EDX mappings of (a)–(a2) SnS_2, (b)–(b2) Fe_2O_3 and (c)–(c4) SnS_2/Fe_2O_3.

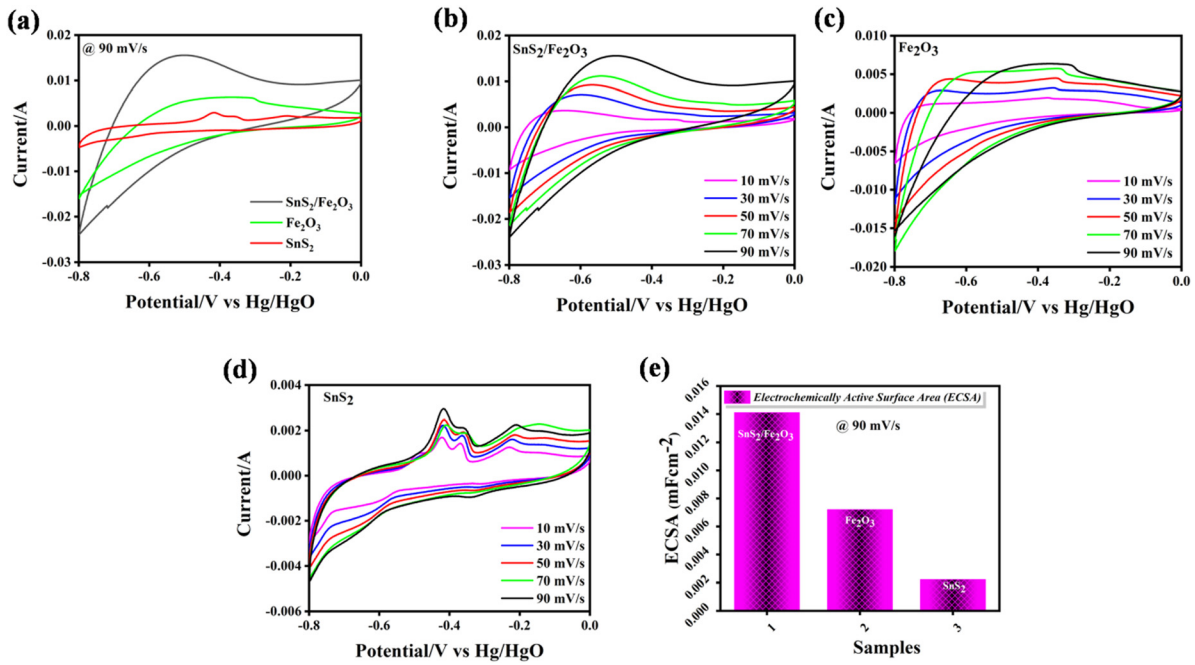

Fig. 7 (a) CV curves of SnS_2/Fe_2O_3, Fe_2O_3 and SnS_2 at 90 mV s^{-1}, (b) CV curves of the SnS_2/Fe_2O_3 composite, (c) CV curves of Fe_2O_3, (d) CV curves of SnS_2 and (e) ECSA of SnS_2/Fe_2O_3, Fe_2O_3 and SnS_2 at 90 mV s^{-1}.

For SnS_2/Fe_2O_3, the redox activity taking place can be written as:

$$\text{Oxidation (at anode): } SnS_2 + 8OH^- \rightarrow SnO_2 + 2SO_4^{2-} + 4H_2O + 6e^- \quad (5)$$

In alkaline solution, Fe_2O_3 can behave as a reduction site. Fe^{3+} can be reduced to Fe^{2+} and metallic iron (Fe):

$$\text{Reduction of } Fe_2O_3 \text{ (cathode): } Fe_2O_3 + 6e^- + 3H_2O \rightarrow 2Fe + 6OH^- \quad (6)$$

Overall, the redox reaction can be written as:

$$SnS_2 + 8OH^- + Fe_2O_3 + 3H_2O + 6e^- \rightarrow SnO_2 + 2SO_4^{2-} + 4H_2O + 6e^- + 2Fe + 6OH^- \quad (7)$$

After e^- cancellation and cancelling OH^- and H_2O:

$$\text{Simplified equation: } SnS_2 + Fe_2O_3 + 2OH^- \rightarrow SnO_2 + 2SO_4^{2-} + 2Fe + H_2O \quad (8)$$

SnS_2 acts as an electron donor, meaning that it is oxidized:

$$Sn^{4+} \rightarrow SnO_2$$

$$S^{2-} \rightarrow SO_4^{2-}$$

Fe_2O_3 acts as an electron accepter meaning that it is reduced:

$$Fe^{3+} \rightarrow Fe^0 \text{ (reduction)}$$

OH^- ions both participate in the oxidation process and neutralize the acidic species. This process show the oxidising behavior of metal sulfides (SnS_2) and reducing behavior of iron oxide (Fe_2O_3).

Furthermore, within the voltage window of −0.8 to 0 V, the various CV curves of the three samples at different scan speeds ranging from 10–90 mV s^{-1} are displayed in Fig. 7(b)–(d). In general, the SnS_2/Fe_2O_3 curves have maintained suitable rectangularity even at high rates of 90 mV s^{-1}, indicating superior capacitive behaviors. Conversely, the CV curves of the SnS_2 and Fe_2O_3 electrodes (Fig. 7c and d) show clear dips and peaks, indicating significantly worse reaction kinetics during the redox reaction. The synergistic interaction between the SnS_2 and Fe_2O_3 phases is responsible for the enhanced response behaviour of SnS_2/Fe_2O_3. The adsorption/desorption of charges on the electrode surface, which primarily depends on the BET surface area, and the redox reaction of the electrode material, which primarily depends on the electrochemical activity of the electrode material, are the two components that make up the capacitance of a supercapacitor. Thus, it is beneficial to obtain the electrochemical surface area from the CV curves (Fig. 7e). Specifically, the high conductivity of SnS_2 and high capacitance of Fe_2O_3 work together to promote ion intercalation and stripping behaviors and produce a two-phase composite that performs better.

To better understand the electrochemical reaction kinetics of SnS_2, Fe_2O_3, and SnS_2/Fe_3O_4, the equation given below was used to fit the relationship between peak current and scan rate in the CV curves:

$$i = aV^b \quad (9)$$

$$\log i = b \log V + \log a \quad (10)$$

Here, V is the scan rate, i is the peak current, and (a) and (b) are coefficients.

In the log(V)–log(i) fitting plot, the y-axis intercept indicates the parameter a, while the slope of the curve indicates parameter b. If the value of parameter b lies between 0 and 0.5, an intercalation process of the ions is involved and diffusion mostly controls the reaction kinetics. Moreover, Faraday reactions, which have pseudocapacitive properties, control the reaction kinetics when b is between 0.5 and 1. The b values of 0.66, 0.62, and 0.58 for SnS_2, Fe_2O_3, and SnS_2/Fe_2O_3, respectively, show that the electrode materials' charge storage mechanism involves both surface capacitance and diffusion-controlled processes. The contribution ratio can be obtained using the formula:

$$i(V) = K_1V + K_2V^{1/2} \quad (11)$$

$$i/V^{1/2} = K_1V^{1/2} + K_2 \quad (12)$$

Using the current separation approach, which Wang[25,26] first proposed, bar charts displaying capacitive and diffusive contributions for the built electrodes at different scan speeds are displayed in Fig. 8a–c. The surface capacitance contribution, which is roughly 40%, is represented by the red integration area in Fig. 8f at a scan rate of 70 mV s^{-1}. As the scan rate is increased from 10 mV s^{-1} to 70 mV s^{-1} (see Fig. 8a–c), the proportion of SnS_2 increases from 9% to 29%, Fe_2O_3 increases from 14% to 36%, and the SnS_2/Fe_2O_3 ratio increases from 18% to 42%. These results show that diffusion-controlled processes dominate the charge storage mechanism at lower scan speeds, suggesting that ions have sufficient time to complete redox reactions. At higher scan rates, however, the impact of surface capacitance increases and the diffusion contribution decreases because ions have less time to come into contact with the electrode material.

GCD experiments were carried out at various current densities of 1–3 A g^{-1} in order to more effectively compare the properties of the three materials. The relevant curves are shown in Fig. 8(a)–(c). Because of the reversible redox reaction, all three samples' curves with various electrodes exhibit a clear charge/discharge plateau and strong symmetry, confirming their pseudocapacitive characteristics. Comparable to the CV results, the composite SnS_2/Fe_2O_3 electrode produced better capacitance properties than the SnS_2 and Fe_2O_3 electrodes, as demonstrated in Fig. 9e and Table 3, with values of 821 A g^{-1}, 297 F g^{-1}, and 170 F g^{-1} at current densities of 1 A g^{-1}, 2 A g^{-1}, and 3 A g^{-1}, respectively. The rough surface of the composite nanoparticles (in Fig. 5c), which provides an extended electrochemical active surface area for the reactions at the electrode/electrolyte interface, may further contribute to the greatest rate performance of SnS_2/Fe_2O_3 (Table 2).

Fig. 10(a) depicts the fitted Nyquist plot for all electrodes, namely SnS_2/Fe_2O_3, SnS_2, and Fe_2O_3. ZSimpWin was employed to analyze the impedance data using a relevant equivalent circuit model. $R_s(Q(C(R_{ct}W)))$, where R_s signifies the solution resistance, "Q" indicates the constant phase element, accounting for the non-ideal capacitive behavior potentially arising from surface flaws or inconsistencies in the electrode material, and "C" denotes the constant phase element (CPE), elucidates the non-ideal capacitive characteristics of the system. It is characterized by two parameters: Q (magnitude) and n (phase angle), with n ranging from 0 to 1. R_{ct} denotes the charge

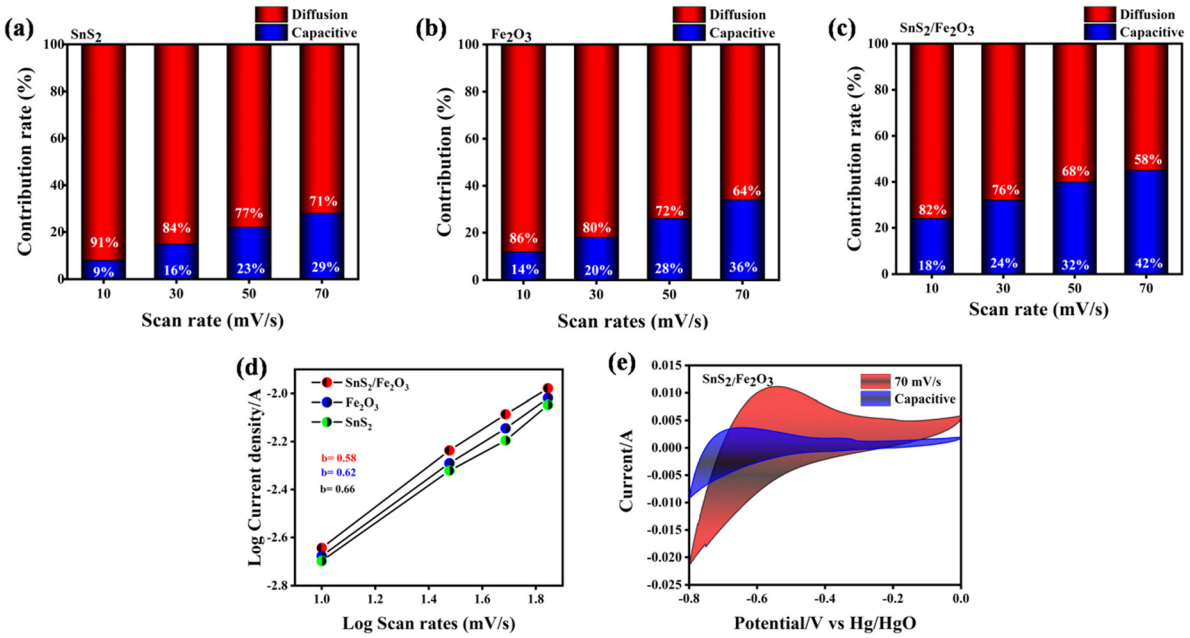

Fig. 8 (a)–(c) Capacitive and diffusion contributions of SnS_2, Fe_2O_3, and the SnS_2/Fe_2O_3 composite, (d) *b*-value of SnS_2/Fe_2O_3, Fe_2O_3 and the SnS_2 composite, and (e) capacitive CV of SnS_2/Fe_2O_3 at 70 mV s^{-1}.

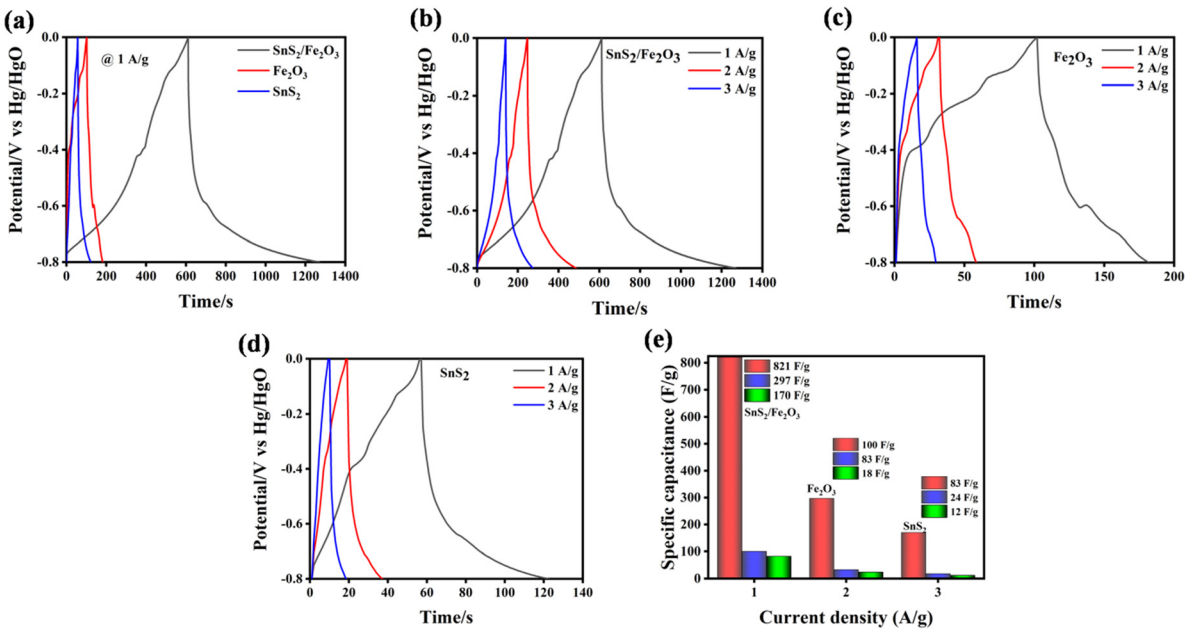

Fig. 9 (a)–(d) GCD curves of all the electrodes, and (e) the specific capacitance *versus* the current density.

transfer resistance, whereas *W* signifies Warburg impedance; the *W* value decreases as Fe_2O_3 presumably develops a more porous or interconnected structure. This facilitates ion transport across the composite, hence lowering the Warburg impedance. The EIS results, which are displayed in Fig. 10 and Table 4, further demonstrate the ion/charge transfer process and quick electrochemical reaction kinetics of the SnS_2/Fe_2O_3 electrode. Generally speaking, the SnS_2/Fe_2O_3 electrode produces values of R_s of 0.53 Ω and R_{ct} of 0.69 Ω, which are less than those of SnS_2 (0.59 Ω, 0.73 Ω) and Fe_2O_3 (0.56 Ω, 0.58 Ω). The three-electrode system's quick charge transfer is the reason for the composite SnS_2/Fe_2O_3 electrode's lowest R_s value, although the SnS_2/Fe_2O_3 electrode's surface has the quickest charge transfer process. In other words, the synergistic impact between the highly-conductive SnS_2 phase and the highly-capacitive Fe_2O_3 phase in the composite should be credited for the desired resistance performance of the composite SnS_2/Fe_2O_3 electrode.

Table 2 Specific capacitance *versus* current density of the composite SnS_2/Fe_2O_3, and pure Fe_2O_3 and SnS_2 samples

Current density (A g^{-1})	SnS_2/Fe_2O_3 (F g^{-1})	Fe_2O_3 (F g^{-1})	SnS_2 (F g^{-1})
1	821	100	83
2	297	33	24
3	170	18	12

Table 3 The electrical resistances of the SnS_2/Fe_2O_3, Fe_2O_3 and SnS_2 electrodes

Sample	SnS_2/Fe_2O_3	Fe_2O_3	SnS_2
R_s (Ω)	0.53	0.56	0.59
R_{ct} (Ω)	0.69	0.58	0.73

6. Electrochemical performances of a two-electrode ASC

In order to assess the SnS_2/Fe_2O_3 electrode's practical viability, a two-electrode ASC was constructed using the SnS_2/Fe_2O_3 and MnO_2 electrodes (Fig. 11a). The MnO_2 electrode's voltage window was 0–0.6 V, whereas the SnS_2/Fe_2O_3 electrode showed a potential window of −0.8 to 0 V (Fig. 10b). CV tests were conducted at scan rates of 10, 30, 50, 70, and 90 mV s^{-1} within the potential window of −1.4 to 0 V (Fig. 11c). The curves output a series of redox peaks at the various scan rates, indicating the typical pseudocapacitive behavior of the SnS_2/Fe_2O_3 electrode and MnO_2 electrode, while the similar shapes of the curves indicate the stability and rate performance of the SnS_2/Fe_2O_3 electrode. Additionally, the GCD results at the various current densities (Fig. 11d) show that the two-electrode ASC provides an energy density of 80.8 Wh kg^{-1} and a specific capacitance of 297 F g^{-1} at 1 A g^{-1}, illustrating the capacitance and energy properties of the device (Fig. 11e and Table 4), which is primarily made possible by the high-performance SnS_2/Fe_2O_3 electrode. The two-electrode ACS was examined using an EIS test in order to investigate its inner resistance and mass transfer behavior. As shown in Fig. 11f, the ACS exhibits a Warburg slope of approximately 45°, indicating moderate ion transfer kinetics following extended work and the structural stability of the two electrodes.

Table 4 Supportive information regarding the capacitance, energy, and power properties at diverse current densities

Current density (A g^{-1})	1	2	3	4	5
Specific capacitance (F g^{-1})	297	63	40.7	31.4	25
Energy density (Wh kg^{-1})	80.8	17.1	11	9	7
Power density (W kg^{-1})	699	1403	2099	2850	3500

Furthermore, following 6000 cycles of charging and discharging at 5 A g^{-1}, respectively, the ACS retained 88% of its initial capacitance (Fig. 12a and b), indicating the perfect stability and structural integrity of the SnS_2/Fe_2O_3 composite electrode. The general performances of the $SnS_2/Fe_2O_3//MnO_2$ ACS are compared with those of the previous work, as listed in Table 5, revealing that the performance is equal to or higher than those of the previous ACSs based on pure SnS_2 or Fe_2O_3 electrodes (the capacitances are determined using the mass of the active materials as a basis) in order to reveal the exceptional properties of SnS_2/Fe_2O_3.

Retention levels of up to 88% at 5 A g^{-1} were obtained from the stability test of the composite SnS_2/Fe_2O_3, which was carried out for 6000 cycles and included the GCD curves displayed in Fig. 12(a). This is consistent with the earlier work. In summary, the previously described composite $SnS_2/Fe_2O_3//MnO_2$ exhibited remarkable capacity retention during prolonged cycling, demonstrating significant stability even after 6000 lengthy cycles. All of the GCD curves showed trends comparable to those of the pristine samples; that is, SnS_2 and Fe_2O_3 retained 78% and 50% of their initial capacities, respectively, even after 6000 cycles, at the same current density. Following the cycling test, the voltage, which is between −0.8 and 0.6 V, did not show any signs of decline. This shows the long-term stability of our asymmetric supercapacitor $SnS_2/Fe_2O_3//MnO_2$ in 6 M KOH aqueous solution electrolyte. Fig. 12(e) displays the energy density *versus* power density curve for the asymmetric supercapacitor $SnS_2/Fe_2O_3//MnO_2$. In asymmetric device investigations, the composite electrode produced a high energy density of roughly 80.8 Wh kg^{-1} at a high power density of 3000 W kg^{-1}, which suggests the valuable performance of our assembled asymmetric supercapacitor.

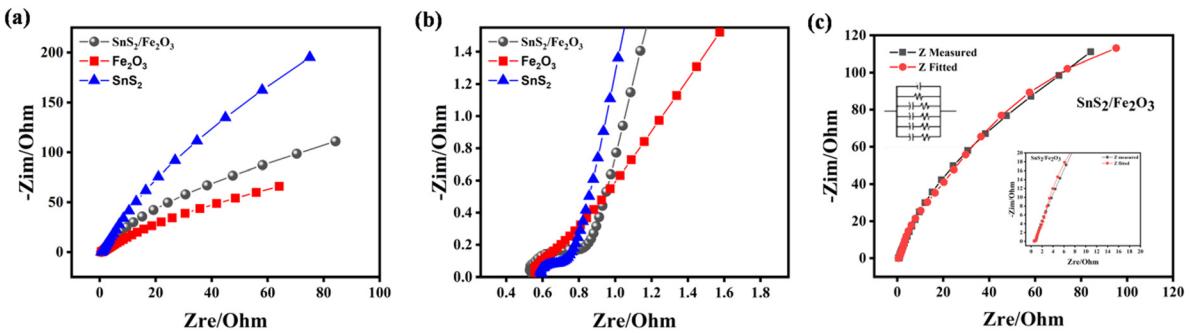

Fig. 10 (a) EIS curves of the SnS_2 electrode, Fe_2O_3 electrode and SnS_2/Fe_2O_3 electrode, (b) locally magnified plots in the three-electrode system and (c) measured and fitted EIS curves of SnS_2/Fe_2O_3.

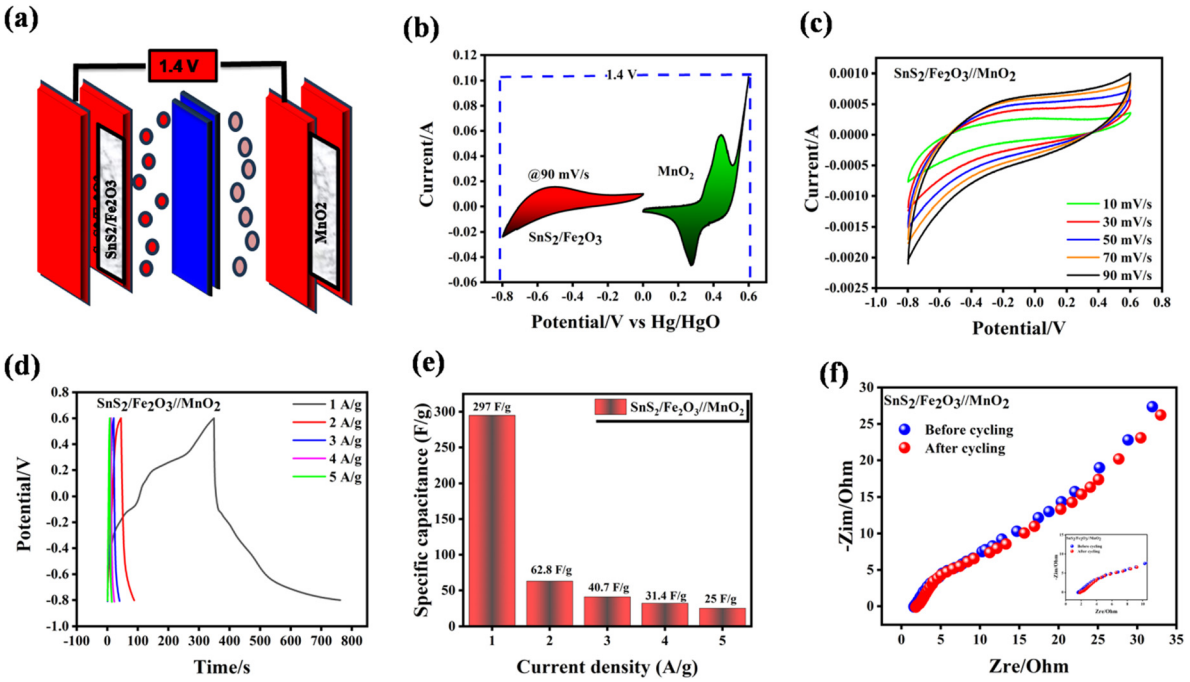

Fig. 11 (a) and (b) Systematic diagram of the two-electrode system with the SnS_2/Fe_2O_3 and MnO_2 electrodes, (c) CV curves at various scan rates, (d) charge/discharge curves at the desired current density, (e) specific capacitance *versus* current density in the two electrode system, and (f) Nyquist plots of $SnS_2/Fe_2O_3//MnO_2$ after the cycling test.

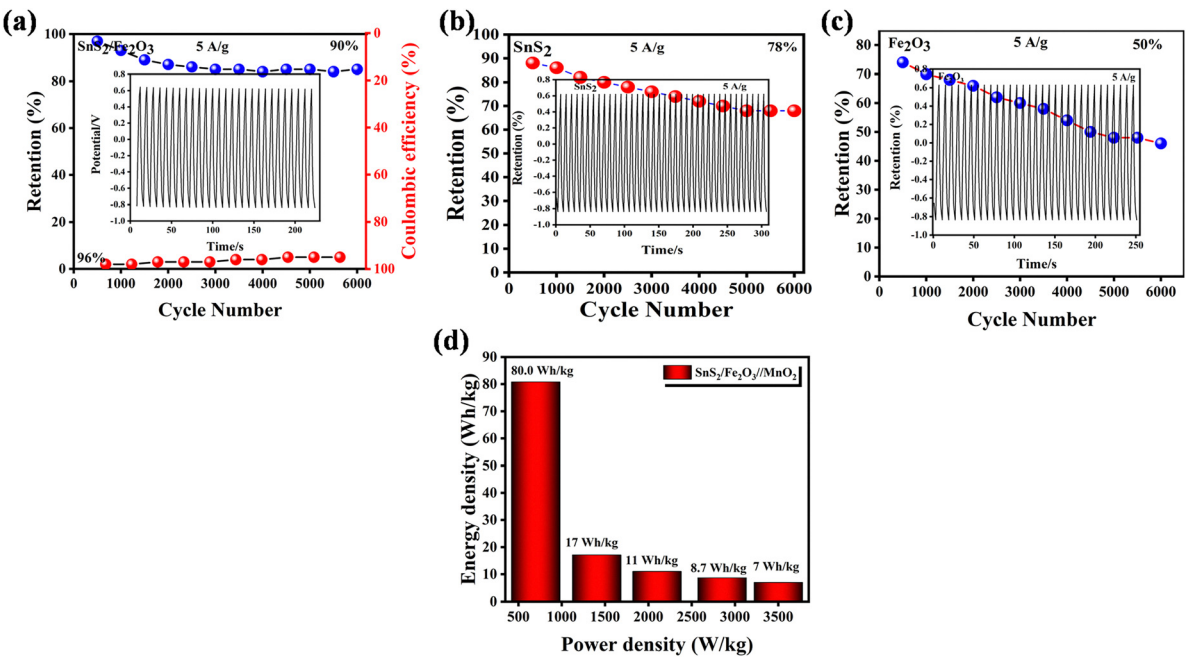

Fig. 12 (a) Retention *versus* cycle number along with coulombic efficiency of the composite SnS_2/Fe_2O_3. (b) and (c) Retention *versus* cycle number test of SnS_2 and Fe_2O_3. (d) Energy density *versus* power density comparison of asymmetric supercapacitor $SnS_2/Fe_2O_3//MnO_2$.

7. Conclusions

In this work, SnS_2/Fe_2O_3 nanocomposites with 40 wt% SnS_2 and 60 wt.% Fe_2O_3 were successfully synthesized by a hydrothermal reaction and wet chemical method for use as an electrode in a high-performance ASC. The synergistic effect between the highly-conductive SnS_2 phase and highly-capacitive Fe_2O_3 phase coordinate well, leading to specific capacitance as high as 821 F g^{-1} in the three-electrode system, higher than those of

Table 5 Ferric oxide electrochemical performance in relation to various composites

Composite	Specific capacitance	Current density (A g^{-1})	Life-span	Capacity retention (%)	Ref.
α-Fe_2O_3	127 F g^{-1}	1	1000	80	27
Fe_2O_3/N-rGO	133.5 F g^{-1}	0.5	5000	56.7	28
rGO/Fe_2O_3	105.4 F g^{-1}	3	2000	74.7	29
NiO//α-Fe_2O_3	57.7 Fg^{-1}	12	10 000	85	30
F–Fe_2O_3	71 F g^{-1}	2.2	15 000	90	31
FeS/Fe_2O_3	154 F g^{-1}	1	500	71	5
TiN/Fe_2O_3	72.5 F g^{-1}	1	10 000	93.7	32
MoO_3–Fe_2O_3//AC	216.7	1	3000	81.1	33
MoS_2/Fe_2O_3/G	98 mAh g^{-1}	1	10 000	77	34
G/Fe_2O_3	378.7 F g^{-1}	1	3000	88.6	35
CF-SnS_2	524.5 F g^{-1}	1	1000	—	36
SnS_2/SnO_2	149 F g^{-1}	2	3000	92	37
SnS_2/Fe_2O_3	297 F g^{-1}	5	6000	88	This work

the pure SnS_2 and Fe_2O_3 systems (82.5 F g^{-1} and 100 F g^{-1}, respectively). Additionally, an ASC with a voltage of 1.4 V delivers the admirable capacity retention of 88% at 5 A g^{-1} after 6000 cycles compared to the pristine samples, where SnS_2 shows 78% and Fe_2O_3 retains just 50%, indicating desirable cycling stability of the pseudocapacitive composite. The ASC exhibits a high energy density of 80.8 Wh kg^{-1} and a power density of 3500 W kg^{-1}, suggesting the practical feasibility of the composite in electrochemical energy storage devices. The power density reflects the rate of energy transfer, while the energy density is an essential metric that quantifies the amount of energy stored per unit mass. The SnS_2/Fe_2O_3 composite is a suitable material for electrochemical energy storage devices due to its elevated energy and power densities. This renders it particularly suitable for applications requiring swift charging and discharging, such as electric vehicles, portable gadgets, and renewable energy systems. The fabrication methodology in this work is anticipated to serve as a pivotal prototype for producing enhanced sulfide-based oxide electrode materials using ball milling and hydrothermal techniques, owing to its exceptional efficacy. It is encouraging for future prospects that further valuable outcomes could be achieved using neutral electrolytes such as K_2SO_4, as optimising the electrolyte is an effective strategy for enhancing energy density.

Author contributions

Wrote the original manuscript draft, data curation: Dost Muhammad. Characterization: Syed Hatim Shah. Supervision, writing – review & editing: Amjad A. Almunyif. Formal analysis: Nisar Ali & Mohammad M. Al-Hinaai. Methodology: Aniqa Jadoon, Rayya Ahmad Al Balushi, Thuraya Al-Harthy. Conceptualization: Sohail Ahmad

Conflicts of interest

The authors declare that they have no conflict of interest.

Data availability

The data used is confidential and will be available on reasonable request.

Acknowledgements

The authors acknowledge the Researchers Supporting Project number (PNURSP2025R901), Princess Nourah bint Abdulrahman University, Riyadh, Saudi Arabia for funding this research work.

References

1 P. Asen and S. Shahrokhian, Ternary nanostructures of Cr_2O_3/graphene oxide/conducting polymers for supercapacitor application, *J. Electroanal. Chem.*, 2018, **823**, 505–516.
2 D. Muhammad, S. H. Shah, S. Elaissi, N. Ali, M. M. Al-Hinaai and S. Ahmad, Facile synthesis of FeS@MoS_2 nanocomposite material: an advantageous electrode for high-performance supercapacitor, *Ionics*, 2025, 1–14.
3 D. Muhammad, X. Liu, H. Hou, X. Yu, J. Rong and J. Riaz, Noval synthesis of systematized FeS/CuO nanostructure efficacious electrode material for escalating asymmetric supercapacitors, *J. Alloys Compd.*, 2025, 178877.
4 D. Muhammad, H. Hou, K. M. Alotaibi, N. Ali, M. M. Al-Hinaai, J. Riaz and A. Safeen, Improved asymmetric supercapacitors using a novel synthesis of organized FeS/SnS_2 nanostructure effective cathode material, *J. Electron. Mater.*, 2025, 1–13.
5 D. Muhammad, X. Liu, H. Hou, Z. Sun, X. Yu, J. Rong and J. Riaz, Well-organized FeS/Fe_2O_3 nanocomposite for the electrode in asymmetric supercapacitors, *J. Electron. Mater.*, 2025, 1–13.
6 M. Talebi, *et al.*, Polyphosphate-reduced graphene oxide on Ni foam as a binder free electrode for fabrication of high performance supercapacitor, *Electrochim. Acta*, 2019, **296**, 130–141.
7 C.-Y. Chen, *et al.*, One-step hydrothermal synthesis of SnS_2/SnO_2/C hierarchical heterostructures for Li-ion batteries anode with superior rate capabilities, *Electrochim. Acta*, 2015, **183**, 78–84.
8 D. H. Lee, *et al.*, Transfer of preheat-treated SnO_2 via a sacrificial bridge-type ZnO layer for ethanol gas sensor, *Sens. Actuators, B*, 2018, **255**, 70–77.
9 M. Haghighi, *et al.*, Surfactant-free stable SnS_2 nanoparticles dispersion for deposition of device-quality films, *Thin Solid Films*, 2019, **669**, 269–274.
10 R. K. Mishra, *et al.*, One-step solvothermal synthesis of carnation flower-like SnS_2 as superior electrodes for supercapacitor applications, *Appl. Surf. Sci.*, 2017, **425**, 923–931.
11 S. Liu, *et al.*, Chemical bath deposition of SnS_2 nanowall arrays with improved electrochemical performance for lithium ion battery, *Mater. Lett.*, 2010, **64**(21), 2350–2353.
12 S. Park, *et al.*, Facile microwave-assisted synthesis of SnS_2 nanoparticles for visible-light responsive photocatalyst, *J. Ind. Eng. Chem.*, 2015, **31**, 269–275.

13 H. Khallaf, *et al.*, Chemical bath deposition of SnO_2 and Cd_2SnO_4 thin films, *Appl. Surf. Sci.*, 2012, **258**(16), 6069–6074.
14 W. Shi and B. Lu, Nanoscale Kirkendall effect synthesis of echinus-like SnO_2@SnS_2 nanospheres as high performance anode material for lithium ion batteries, *Electrochim. Acta*, 2014, **133**, 247–253.
15 X. Peng, *et al.*, Two dimensional nanomaterials for flexible supercapacitors, *Chem. Soc. Rev.*, 2014, **43**(10), 3303–3323.
16 X. Lu, *et al.*, Oxygen-deficient hematite nanorods as high-performance and novel negative electrodes for flexible asymmetric supercapacitors, *Adv. Mater.*, 2014, **26**(19), 3148–3155.
17 Y. Abbas, *et al.*, Anchoring 2D $NiMoO_4$ nano-plates on flexible carbon cloth as a binder-free electrode for efficient energy storage devices, *Ceram. Int.*, 2020, **46**(4), 4470–4476.
18 K. Krishnamoorthy, *et al.*, Designing two dimensional nanoarchitectured MoS_2 sheets grown on Mo foil as a binder free electrode for supercapacitors, *Electrochim. Acta*, 2016, **190**, 305–312.
19 S. Ghasemi, S. R. Hosseini and P. Asen, Preparation of graphene/nickel-iron hexacyanoferrate coordination polymer nanocomposite for electrochemical energy storage, *Electrochim. Acta*, 2015, **160**, 337–346.
20 Z. Fan, *et al.*, Asymmetric supercapacitors based on graphene/MnO_2 and activated carbon nanofiber electrodes with high power and energy density, *Adv. Funct. Mater.*, 2011, **21**(12), 2366–2375.
21 J. Cai, *et al.*, 3 electrons donator-FeS/C composite anode for supercapacitor, *J. Mater. Sci.: Mater. Electron.*, 2022, **33**(36), 26966–26979.
22 K. C. Christoforidis, A. Sengele, V. Keller and N. Keller, Single-step synthesis of SnS_2 nanosheet-decorated TiO_2 anatase nanofibers as efficient photocatalysts for the degradation of gas-phase diethylsulfide, *ACS Appl. Mater. Interfaces*, 2015, **7**, 19324–19334.
23 K. Ye, Y. Li, H. Yang, M. Li, Y. Huang, S. Zhang and H. Ji, An ultrathin carbon layer activated CeO_2 heterojunction nanorods for photocatalytic degradation of organic pollutants, *Appl. Catal., B*, 2019, **259**, 118085.
24 C. W. Wu, B. Unnikrishnan, I. W. P. Chen, S. G. Harroun, H. T. Chang and C. C. Huang, Excellent oxidation resistive MXene aqueous ink for micro-supercapacitor application, *Energy Storage Mater.*, 2020, **25**, 563–571.
25 G. Wang, L. Zhang and J. Zhang, A review of electrode materials for electrochemical supercapacitors, *Chem. Soc. Rev.*, 2012, **41**(2), 797–828.
26 Y. Li, Y. Xia, K. Liu, K. Ye, Q. Wang, S. Zhang and H. Liu, Constructing Fe-MOF-derived Z-scheme photocatalysts with enhanced charge transport: nanointerface and carbon sheath synergistic effect, *ACS Appl. Mater. Interfaces*, 2020, **12**(22), 25494–25502.
27 S. Shivakumara, T. R. Penki and N. Munichandraiah, Synthesis and characterization of porous flowerlike α-Fe_2O_3 nanostructures for supercapacitor application, *ECS Electrochem. Lett.*, 2013, **2**(7), A60.
28 Y. Cheng, *et al.*, Substrate bias dependence of Raman spectra for TiN films deposited by filtered cathodic vacuum arc, *J. Appl. Phys.*, 2002, **92**(4), 1845–1849.
29 H. Liu, *et al.*, Easy one-step hydrothermal synthesis of nitrogen-doped reduced graphene oxide/iron oxide hybrid as efficient supercapacitor material, *J. Solid State Electrochem.*, 2015, **19**, 135–144.
30 J. Wang, J. Polleux, J. Lim and B. Dunn, Pseudocapacitive contributions to electrochemical energy storage in TiO_2 (anatase) nanoparticles, *J. Phys. Chem. C*, 2007, **111**, 14925–14931.
31 Y. Hu, *et al.*, Hybrid Fe_2O_3 nanoparticle clusters/rGO paper as an effective negative electrode for flexible supercapacitors, *Chem. Mater.*, 2016, **28**(20), 7296–7303.
32 J. Riaz, Y. Zhang, J. Cao, A. Bibi, M. Arif, Z. Zhang and X. Zhou, Facile synthesis of TiN nanosheets decorated Fe_2O_3 nanoparticles as novel cathode material for asymmetric supercapacitor, *Surf. Interfaces*, 2024, **46**, 104080.
33 S. Sundaresan, D. Subramanian and G. Raju, Exploration of two-dimensional MoO_3-Fe_2O_3 nanocomposite for the fabrication of high energy density supercapacitor applications, *Inorg. Chem. Commun.*, 2023, **148**, 110360.
34 R. Palanisamy, D. Karuppiah, S. Venkatesan, S. Mani, M. Kuppusamy, S. Marimuthu and R. Perumalsamy, High-performance asymmetric supercapacitor fabricated with a novel MoS_2/Fe_2O_3/graphene composite electrode, *Colloid Interface Sci. Commun.*, 2022, **46**, 100573.
35 W. Gao, Y. Li, J. Zhao, Z. Zhang, W. Tang, J. Wang and Z. Li, Design and preparation of graphene/Fe_2O_3 nanocomposite as negative material for supercapacitor, *Chem. Res. Chin. Univ.*, 2022, **38**(4), 1097–1104.
36 R. K. Mishra, G. W. Baek, K. Kim, H. I. Kwon and S. H. Jin, One-step solvothermal synthesis of carnation flower-like SnS_2 as superior electrodes for supercapacitor applications, *Appl. Surf. Sci.*, 2017, **425**, 923–931.
37 P. Asen, M. Haghighi, S. Shahrokhian and N. Taghavinia, One step synthesis of SnS_2-SnO_2 nano-heterostructured as an electrode material for supercapacitor applications, *J. Alloys Compd.*, 2019, **782**, 38–50.

